

A method for estimating the spatial coherence of mid-latitude skywave propagation based on transionospheric scintillations at 35 MHz

Joseph F Helmboldt¹

¹Naval Research Laboratory

December 7, 2022

Abstract

The results of a study aimed at assessing the utility of transionospheric 35 MHz scintillation measurements toward cosmic radio sources for estimating the level of spatial coherence in high frequency (HF) skywave systems are presented. This was done using an array of four antennas in southern Maryland called the Deployable Low-band Ionosphere and Transient Experiment (DLITE). Two of the antennas within a ~350-m north/south baseline were used to monitor 35-MHz intensity variations of two bright cosmic sources, Cynus A and Cassiopeia A. The other two antennas, which were within a ~420-m east/west baseline, recorded the 7.85 MHz skywave from the CHU radio station near Ottawa, Ontario. These HF measurements were used to quantify the level of spatial coherence by measuring the amplitudes of the cross correlation of the two antennas' recorded voltages relative to the received power, which were typically ~0.5-0.9, but occasionally near zero. A method was developed to estimate the expected cross-correlation amplitude based on the 35-MHz scintillations. This method assumes the case of weak scattering, which is generally appropriate for mid-latitudes, and that the irregularity distribution follows that of the background electron density. These calculations typically captured the day-to-day variations in spatial coherence quite well (correlation coefficient $r \approx 0.6$) while only marginally reproducing hour-to-hour variations ($r \approx 0.2$). Thus, this method holds promise as an economical and passive means to assess the spatial coherence expected for skywave propagation within a given mid-latitude region.

Abstract

The results of a study aimed at assessing the utility of transionospheric 35 MHz scintillation measurements toward cosmic radio sources for estimating the level of spatial coherence in high frequency (HF) skywave systems are presented. This was done using an array of four antennas in southern Maryland called the Deployable Low-band Ionosphere and Transient Experiment (DLITE). Two of the antennas within a ~ 350 -m north/south baseline were used to monitor 35-MHz intensity variations of two bright cosmic sources, Cynus A and Cassiopeia A. The other two antennas, which were within a ~ 420 -m east/west baseline, recorded the 7.85 MHz skywave from the CHU radio station near Ottawa, Ontario. These HF measurements were used to quantify the level of spatial coherence by measuring the amplitudes of the cross correlation of the two antennas' recorded voltages relative to the received power, which were typically ~ 0.5 – 0.9 , but occasionally near zero. A method was developed to estimate the expected cross-correlation amplitude based on the 35-MHz scintillations. This method assumes the case of weak scattering, which is generally appropriate for mid-latitudes, and that the irregularity distribution follows that of the background electron density. These calculations typically captured the day-to-day variations in spatial coherence quite well (correlation coefficient $r \simeq 0.6$) while only marginally reproducing hour-to-hour variations ($r \simeq 0.2$). Thus, this method holds promise as an economical and passive means to assess the spatial coherence expected for skywave propagation within a given mid-latitude region.

1 Introduction

For just over a century, refraction of medium frequency (MF; 0.3–3 MHz) and high frequency (HF; 3–30 MHz) radio waves within the ionosphere has offered a reasonably low-loss (especially at night) pathway for over-the-horizon (OTH) communications and radar-based surveillance. This so-called “skywave” propagation offered one of the first means of global wireless radio communication. Even in an age of replete with satellite-based systems, skywave HF comms and OTH radars continued to be exploited as economical means for long-range transmissions and surveillance of large areas from far away.

The ionosphere is not a static medium, however, and so this approach is not without drawbacks. Disturbances and irregularities on scales from a few meters to thousands of kilometers occur and can cause various deleterious effects on skywave systems. Because they are comparable to the Fresnel scale for ground-based HF systems, km-scale irregularities can be especially problematic. Such irregularities cause phase and intensity variations that can, for instance, broaden Doppler signatures within OTH radars and, in some cases, cause a complete loss of temporal or spatial coherence. The latter is of particular concern for systems that rely on arrays of receiving antennas since they require at least some level of coherence among the array elements. Thus, having a detailed assessment of the ionospheric coherence length within a given region is important for both site selection and design of array-based skywave systems.

Such an assessment is not always practical and/or economical with shortwave systems, especially if coverage within a relatively large region is desired. At low and high latitudes, irregularity activity is typically high enough that satellite-based microwave beams, e.g., Global Positioning System (GPS) signals, can be used to estimate parameters such as the coherence length and extrapolate to the HF regime. Consequently, GPS scintillations have been used for decades to study ionospheric irregularities within these regions (for a review, see Kintner et al. (2007)).

At mid-latitudes, irregularity activity tends to be quite low by comparison. Because the impact of these structures is stronger the closer the operating frequency is to the ionospheric plasma frequency (usually ~ 1 – 10 MHz), scintillations at mid-latitudes are rarely visible at microwave frequencies. At lower frequencies ($\lesssim 100$ MHz), scintillations are nearly always present, but there are few if any satellite-based transmitters within this frequency

64 regime. Cosmic radio sources offer an alternative as many of these objects have spec-
 65 tra that increase in intensity at lower frequency (due to, e.g., synchrotron emission). In-
 66 deed, there is a growing body of work of radio telescope-based measurements used to study
 67 ionospheric disturbances toward cosmic radio sources (e.g., Jacobson and Erickson (1992);
 68 Cohen and Röttgering (2009); Helmboldt et al. (2012); Loi et al. (2015); Helmboldt and
 69 Hurley-Walker (2020)). In particular, Mevius et al. (2016) demonstrated that scintilla-
 70 tions at low frequencies toward bright cosmic radio sources are always present. Because
 71 interferometers are often used within radio astronomy for high angular resolution imag-
 72 ing, especially at lower frequencies, the coherence length is an important quantity for tele-
 73 scope design and siting as well. This is especially true given recent efforts to push to lower
 74 frequencies in search of signatures of the so-called Cosmic Dawn, which are related to
 75 a reduction in emission from neutral hydrogen in the early universe due to photoioniza-
 76 tion by the first stars (e.g., DiLullo et al. (2020)).

77 In an effort to build on successes with radio astronomy-based ionospheric measure-
 78 ments while circumventing the portability limitations of large radio telescopes, a new low-
 79 cost telescope array, optimized for ionospheric remote sensing, was recently developed.
 80 This Deployable Low-band Ionosphere and Transient Experiment (DLITE) consists of
 81 four antennas that monitor a small number of exceptionally bright cosmic radio sources
 82 at 35 MHz for ionospheric variations in both intensity and phase (Helmboldt et al., 2021).
 83 The study presented here was focused on using a DLITE array in southern Maryland
 84 in a novel mode to assess the utility of transionospheric 35 MHz scintillation measure-
 85 ments to characterize the expected spatial coherence of an HF skywave signal. To test
 86 this, the 7.85 MHz carrier wave of the CHU radio station near Ottawa, Ontario received
 87 at the Maryland site was also recorded and analyzed. The experimental setup and re-
 88 sults of a data collection campaign from Oct./Nov. 2020 are detailed in Sec. 2 while the
 89 method for converting 35-MHz scintillation measurements to 7.85 coherence estimates
 90 is described in Sec. 3. Results are summarized and discussed in Sec. 4.

91 2 Experiment Design and Observations

92 Data were obtained within a novel collection mode utilizing a DLITE system de-
 93 ployed near Pomonkey, Maryland (DLITE-POM for short). A thorough description of
 94 the DLITE system and the methods developed to analyze the data it produces is given
 95 by Helmboldt et al. (2021). In brief, DLITE is a radio telescope array of four antennas,
 96 which were originally designed for the Long Wavelength Array (LWA) project (Taylor
 97 et al., 2012; Ellingson et al., 2013). They are bowtie-shaped, bent dipole antennas with
 98 active baluns that make them sky noise-dominated (by 6 dB or more) in the 20-80 MHz
 99 range (Hicks et al., 2012). DLITE employs these antennas as an interferometer connected
 100 to a digital backend composed of mostly commercial off-the-shelf (COTS) parts, includ-
 101 ing widely used Ettus-brand software defined radios. This backend continuously cross-
 102 correlates all six unique baselines within the array. To avoid the relatively large num-
 103 ber of antennas needed for beam forming with phased arrays, DLITE uses time and fre-
 104 quency difference of arrival (TDOA and FDOA) to resolve individual cosmic radio sources
 105 from one another. This is enabled by relatively long baselines (~ 200 – 500 m) and large
 106 bandwidth (~ 6 – 10 MHz).

107 DLITE-POM was deployed in the summer/fall of 2019, in part to support the Space
 108 Measurement of a Rocket-released Turbulence (SMART) experiment (Ganguli et al., 2019;
 109 Fletcher et al., 2020). With help from colleagues at the University of New Mexico, a sec-
 110 ond array was established at the site of the Very Large Array (VLA) near Datil, New
 111 Mexico by repurposing existing but dormant LWA antennas. A third array was deployed
 112 at Malabar Annex Space Force Base near Melbourne, Florida in Nov. 2021 in cooper-
 113 ation with the 45th Space Wing.

114 For the SMART experiment, methods were developed to use DLITE as a scintil-
 115 lometer. Considering various factors, it was found that the optimum band for scintilla-
 116 tion measurements is 30–40 MHz. These rely on the generation of TDOA/FDOA im-
 117 ages from each of the array’s six baselines. For each baseline, a particular cosmic source
 118 has a predictable TDOA and FDOA. For the fractional bandwidth used by DLITE (~24%),
 119 the equivalent resolution on the sky for TDOA and FDOA are the same for an integra-
 120 tion time of about one hour. In practice, windowing reduces the temporal resolution to
 121 ~30 minutes. Within these images, scintillations create a plateau-like artifact in the FDOA
 122 direction only, the magnitude of which is $= \sigma_I / \sqrt{N_t}$, where σ_I is the intensity standard
 123 deviation and N_t is the number of time steps used to generate the TFOA/FDOA im-
 124 age. Thus, the peak intensity relative to this artifact can be used to measure the S_4 scin-
 125 tillation index, which is the ratio of σ_I to the mean intensity. Combining the S_4 index
 126 with the observing geometry yields the irregularity index, $C_k L$, which is proportional
 127 to the vertically integrated electron density variance.

128 According to Rino (1979); Carrano et al. (2019); Helmboldt et al. (2021), for fre-
 129 quencies well above the plasma frequency, the S_4 index is related to $C_k L$ by

$$S_4 = \frac{\sigma_I}{I} \quad (1)$$

$$\sigma_I^2 = I^2 \frac{C_k L}{\sin e} (r_e \lambda)^2 \left(\frac{2\pi}{1000} \right)^{2\nu+1} \left(\frac{z_R \lambda}{2\pi \sin e} \right)^{\nu-0.5} \frac{\wp(\nu) F_S(\nu)}{D_S} + \sigma_{sys}^2 \quad (2)$$

$$F_S(\nu) = \frac{\Gamma(1.25 + \nu/2)}{2^{\nu+0.5} \sqrt{\pi} \Gamma(\nu/2 + 0.25) (\nu - 0.5)} \quad (3)$$

130 with all quantities specified in MKS units. In equation (2), r_e is the classical electron
 131 radius, z_R is the irregularity height, σ_{sys} is the system noise (including external/sky noise),
 132 and \wp is a geometric and propagation factor that depends on the orientation of the ir-
 133 regularities relative to the line of sight. For mid-latitudes, it is generally a good assump-
 134 tion that the irregularities are aligned along magnetic field lines with major/minor axis
 135 ratios of about 10:1, which is what is assumed for DLITE analysis. The irregularities are
 136 also assumed to be at a height of 300 km, but the dependence on assumed height is rel-
 137 atively weak ($\propto z_R^{0.85}$). The shape of the irregularity spectrum is represented by ν , which
 138 is assumed to be 1.35 to approximate Kolmogorov turbulence (Tatarskii, 1961). The ob-
 139 serving wavelength is λ , and e is the elevation angle of the line of sight. The factor D_S
 140 is unique to DLITE and accounts for the fact that none of the observed A-Team sources
 141 are point-like. The derivation of this value per source is described by Helmboldt et al.
 142 (2021).

143 For this study, the DLITE-POM array was run in a novel mode where only two an-
 144 tennas, those within a relatively long north/south baseline (~350 m), were cross-correlated
 145 in the normal way and used to generate TDOA/FDOA images for scintillometry at 35
 146 MHz. The other two antennas form a ~420-m east/west baseline and were used to record
 147 raw complex voltages at 7.85 MHz with 2.5 kHz of bandwidth to monitor the skywave
 148 propagated signal from CHU. The linear polarization voltages at 7.85 MHz were con-
 149 verted to right- and left-handed circular polarization (RHCP and LHCP, respectively),
 150 and cross-correlated after the fact with a coherent integration time of 1.2 s. We note that
 151 even in this novel mode, all eight channels of the system (four antennas, two polariza-
 152 tions each) were synched to the same 10 MHz reference and pulse per second signal dur-
 153 ing all collections, as usual (see Helmboldt et al. (2021)). Collections in this mode were
 154 performed every day from 2 Oct. through 1 Nov. 2020 from 17–23 UT each day (except
 155 1 Nov., for which data was collected 18–24 UT) to maximize the time that the 7.85 MHz
 156 CHU signal was detectable from Pomonkey and when the two brightest cosmic 35 MHz
 157 sources, Cygnus A and Cassiopeia A (Cyg A and Cas A), were visible.

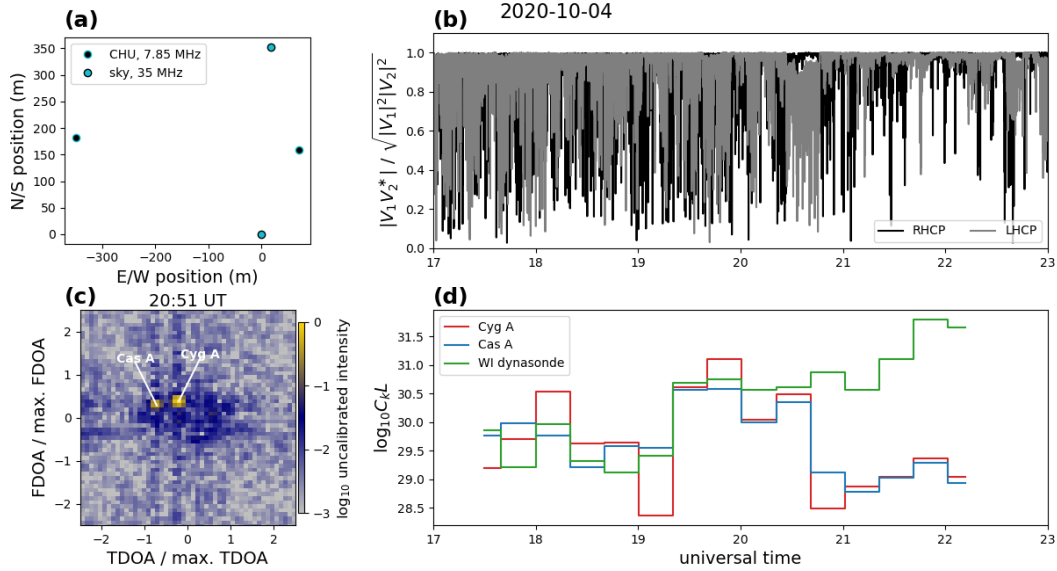


Figure 1. An example of the data products generated from the observing campaign. (a) The layout of the DLITE-POM antennas. The antennas used for 35-MHz sky observations are represented by cyan dots; those used to record the 7.85 MHz CHU skywave are represented by black dots. (b) The cross-correlation amplitude between the two antennas used to record the CHU skywave as a function of time within 1.2-s integrations. Right- and left-hand circular polarization (RHCP and LHCP) are plotted in black and gray, respectively. (c) A time and frequency difference of arrival (TDOA and FDOA) image of the sky at 35 MHz from the data collected with the north/south baseline shown in panel (a). The locations of the two bright sources Cyg A and Cas A are indicated. (d) Time series of the $C_k L$ irregularity index extracted from the 35 MHz data for Cyg A (red) and Cas A (blue) as well as estimates from parameters take from the Wallops Island (WI) dynasonde (green; see Sec. 2).

158 This observing mode and its data products are illustrated in Fig. 1 which shows
 159 for 4 Oct. 2020 (a) the antenna layout, including which antennas were used for which
 160 measurements, (b) the cross-correlation amplitude of the CHU 7.85 MHz signals rela-
 161 tive to the received power, (c) one of 15 TDOA/FDOA images of the sky at 35 MHz,
 162 and (d) $C_k L$ derived from Cyg A (red) and Cas A (blue). Within panel (b), one can see
 163 the plateau-like FDOA artifacts reference above (in blue) used to characterize the level
 164 of scintillations. The resulting $C_k L$ values are mostly higher prior to 21 UT after which
 165 they drop somewhat, although with some level of disagreement between the two sources.
 166 Likewise, the spatial coherence of the 7.85 MHz signal tended to be lower prior to 21 UT
 167 and higher afterward (i.e., the coherence should be lower when $C_k L$ is larger).

168 Following the analysis of Helmboldt and Zobotin (2022), parameters were also ob-
 169 tained from the Wallops Island (WI) dynasonde radar system, which is ~ 160 km south-
 170 east of Pomonkey. Automatically generated parameters that characterize the peak plasma
 171 frequency, peak height, scale height, and km-scale irregularity spectrum for the E- and
 172 F-regions separately were used. Helmboldt and Zobotin (2022) showed that combining
 173 these parameters while assuming the irregularities follow the N_e profile with Chapman
 174 layers per region yielded estimates of $C_k L$ that were in good agreement with measure-
 175 ments made with DLITE-POM. The green curve in Fig. 1d shows $C_k L$ computed in this
 176 way, averaged within the same time intervals used for the DLITE-POM measurements.
 177 One can see that they agree rather well up until just before 21 UT, where the DLITE
 178 $C_k L$ drops and the WI values rise somewhat. This is in contrast with the CHU 7.85 MHz
 179 signal, which becomes more spatially coherent during this time, implying that there may
 180 have been somewhat localized irregularity activity near WI at that time.

181 3 Spatial Coherence Calculations

182 This section provides details regarding the model used to compute estimates of spa-
 183 tial coherence constrained with DLITE-based $C_k L$ measurements. This is a modified ver-
 184 sion of the single-layer model published by Rino (1979), and it is therefore refer to as
 185 the MR79 model for short. The original model was designed for transionospheric prop-
 186 agation of radio signals at frequencies much higher than the plasma frequency. The MR79
 187 version contains additional terms meant to adapt it to skywave propagation where the
 188 signals do not leave the bottom-side of the ionosphere and are at frequencies larger than,
 189 but similar to, the plasma frequency.

190 3.1 Model Derivation

191 The derivation of the model published by Rino (1979) begins with a relationship
 192 between the change in phase of a radio signal, $\delta\phi$, due to a perturbation in the ionospheric
 193 electron density, ΔN_e , which assumes $f \gg f_p$, where f_p is the plasma frequency $= c\sqrt{N_e r_e/\pi}$.
 194 More generally, $\delta\phi$ can be related to a change in the index of refraction, $N = \sqrt{1 - (f_p/f)^2}$,
 195 namely

$$\delta\phi = \frac{2\pi}{\lambda} \int_0^\infty \Delta N ds \quad (4)$$

196 where ds is along a particular line of sight/propagation path. In the weak scattering case,
 197 the change in N is relatively small, and equation (5) can be approximated as

$$\delta\phi \simeq -r_e \lambda \int_0^\infty \frac{\Delta N_e}{N} ds \quad (5)$$

198 In this context, weak scattering refers to irregularity-driven changes in the electron
 199 density, ΔN_e , that are small enough that the approximation given in equation (5) is still

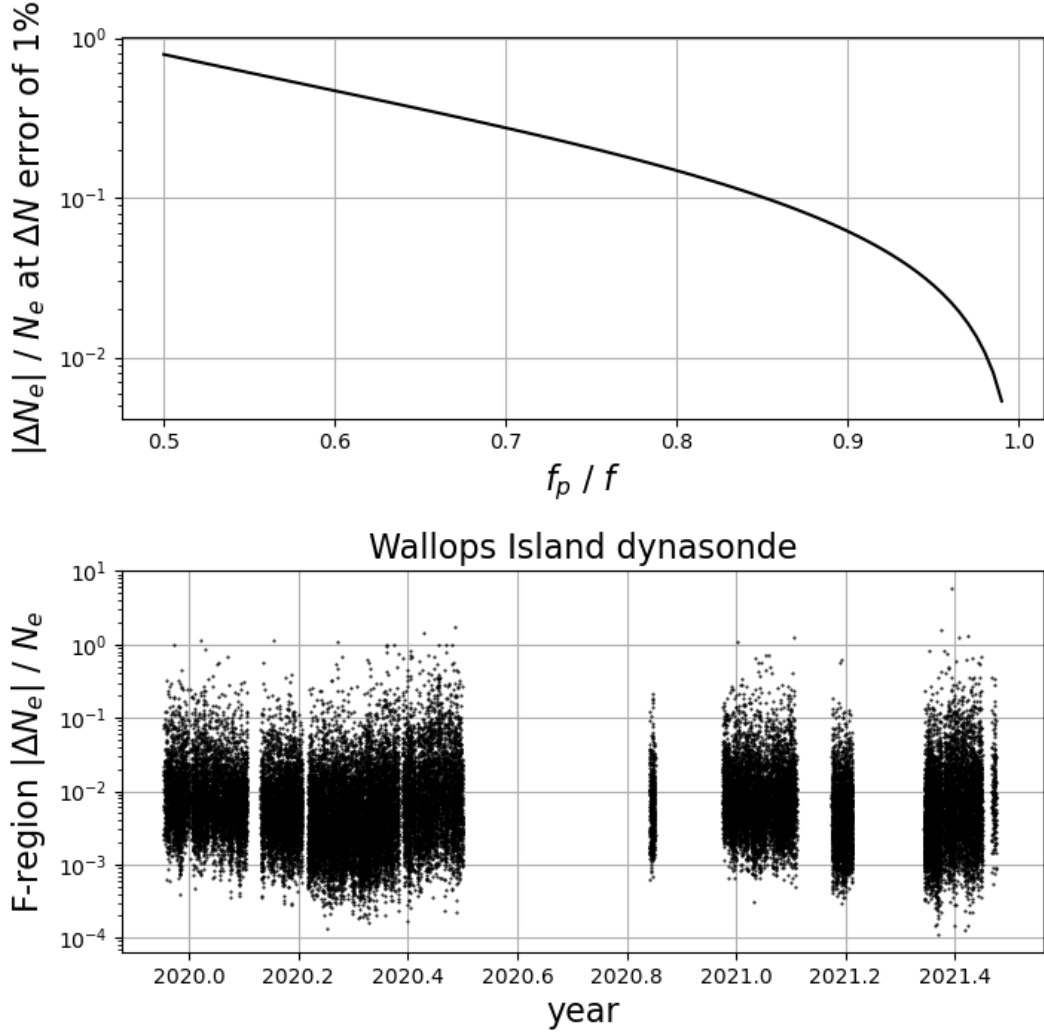


Figure 2. Upper: The relative standard deviation in the electron density, $|\Delta N_e|/N_e$, that causes an error of 1% for the resulting change in the index of refraction, ΔN , calculated from the approximation in equation (6) versus the ratio of the plasma frequency to the observing frequency. Lower: A time series of estimates of $|\Delta N_e|/N_e$ from F-region irregularity parameters measured with the dynasonde system near Wallops Island, Virginia

200 valid. The upper panel of Fig. 2 shows the value of $|\Delta N_e|/N_e$ that will cause this ap-
 201 proximation to be off by 1% as a function of f_p/f . From this curve, one can see that for
 202 $f_p/f < 0.9$, relative N_e deviations of up to around 7% qualify as weak within this con-
 203 text. For lower f_p/f ratios, that limit can be much higher (e.g., $\sim 80\%$ at $f_p/f = 0.5$).
 204 Following the analysis presented in Helmboldt and Zabolin (2022), irregularity param-
 205 eters measured with the WI dynasonde were used to estimate the F-region $|\Delta N_e|/N_e$ from
 206 Dec. 2019 through Jun. 2021, and the results are plotted in the lower panel of Fig. 2. The
 207 vast majority of these estimates (97%) are below 7%. Note that for $f \simeq f_p$, this ap-
 208 proximation cannot hold, which is why vertical sounders like the WI dynasonde must
 209 be treated differently. For a thorough discussion of this special case, see Zabolin and Wright
 210 (2001).

211 For $f \gg f_p$, $N \simeq 1$ everywhere, and equation (5) is the same as equation (1) of
 212 Rino (1979). For skywave propagation, this same assumption cannot be made. However,
 213 equation (5) illustrates that irregularities near the reflection height where N is at a min-
 214 imum within the propagation path will have an outsized impact. Thus, even though ir-
 215 regularities may be distributed throughout the ionosphere, in this case, their impact can
 216 be approximated by assuming a single layer near the reflection height since those carry
 217 the largest weight. In this case, the value of N in the integrand of equation (5) can be
 218 fixed at $\sqrt{1 - (f_{p,max}/f)^2}$, where $f_{p,max}$ is the plasma frequency at the reflection height,
 219 and moved outside the integral.

220 This implies that the relationship derived by Rino (1979) between the phase vari-
 221 ance/covariance and the ΔN_e power spectrum can be adapted to be appropriate for sky-
 222 wave propagation by dividing by a factor of $1 - (f_{p,max}/f)^2$ (i.e., N_{min}^2). Furthermore,
 223 for a virtual mirror approximation, $f_{p,max}/f \simeq \cos \theta$, where θ is the zenith angle of the
 224 propagation vector, and so multiplying by $\csc^2 \theta$ will have a similar effect. Additionally,
 225 the signal does not propagate through the full ionosphere, and so only part of the irreg-
 226 ularity distribution contributes to the phase variance/covariance. As supported by the
 227 results of Helmboldt and Zabolin (2022), one can assume that the irregularities follow
 228 the N_e distribution. The HF propagation simulator of Nickisch et al. (2012) also makes
 229 this same assumption. It then follows that the equations from Rino (1979) can be scaled
 230 by a factor $F_e = \left(\int_0^{h_{max}} N_e^2 dz \right) \left(\int_0^\infty N_e^2 dz \right)^{-1}$, where h_{max} is the reflection height. This
 231 can be calculated numerically using a specified N_e profile. Finally, for skywave propa-
 232 gation, the irregularity layer is effectively traversed twice for each ‘‘hop’’ of the signal,
 233 implying that an additional factor of $2N_{hop}$ must also be included.

234 Taking into account the modifications described above, the correlation function of
 235 phase variations within the MR79 model is given by

$$R_{\delta\phi}(r_{eff}) = C' \left| \frac{r_{eff}}{2q_0} \right|^{\nu-1/2} \frac{K_{\nu-1/2}(q_0 r_{eff})}{2\pi\Gamma(\nu+1/2)} \quad (6)$$

$$C' \equiv [2N_{hop}F_e \csc^2 \theta] Gr_e^2 \lambda^2 \sec \theta \left(\frac{2\pi}{1000} \right)^{2\nu+1} C_k L \quad (7)$$

236 where the terms within the first set of brackets in the definition of C' are the new ones
 237 added here, and the remainder are from equation (12) of Rino (1979). The G term is a
 238 geometrical factor described by Rino (1979), which depends on the azimuth of the propa-
 239 gation direction. The quantity $q_0 = 2\pi/L_0$, where L_0 is the outer scale, usually as-
 240 sumed to be about 30 km (Nickisch et al., 2012). The spectral shape ν is the same as
 241 that discussed in Sec. 2. This gives the phase covariance for two locations with an ef-
 242 fective one-dimensional separation of r_{eff} , which takes into account the irregularity ori-
 243 entations and shapes as defined by Rino (1979). For the two antennas at DLITE-POM
 244 used to collect 7.85 MHz CHU data and the geometry of the propagation path (see Sec.
 245 3.2), $r_{eff} \simeq 220$ m.

246 The phase of the cross correlated signal will have a variance given by the structure
 247 function, which is the variance in the difference in phase, $\Delta\phi$, between to points sepa-
 248 rated by r_{eff} . Since the antennas used are significantly closer together than the outer
 249 scale, the scale-free approximation can be used, which is given by Rino (1979); Carrano
 250 et al. (2019) and modified here to be

$$\sigma_{\Delta\phi}^2 \simeq C' \frac{2\Gamma(3/2 - \nu)}{2\pi\Gamma(\nu+1/2)(2\nu-1)2^{2\nu-1}} r_{eff}^{2\nu-1} \quad (8)$$

251 which is valid for $1/2 < \nu < 3/2$. The amplitude of the cross correlated signal will then
 252 be reduced by a factor of $\exp(-\sigma_{\Delta\phi}^2/2)$. This can be measured directly by normalizing

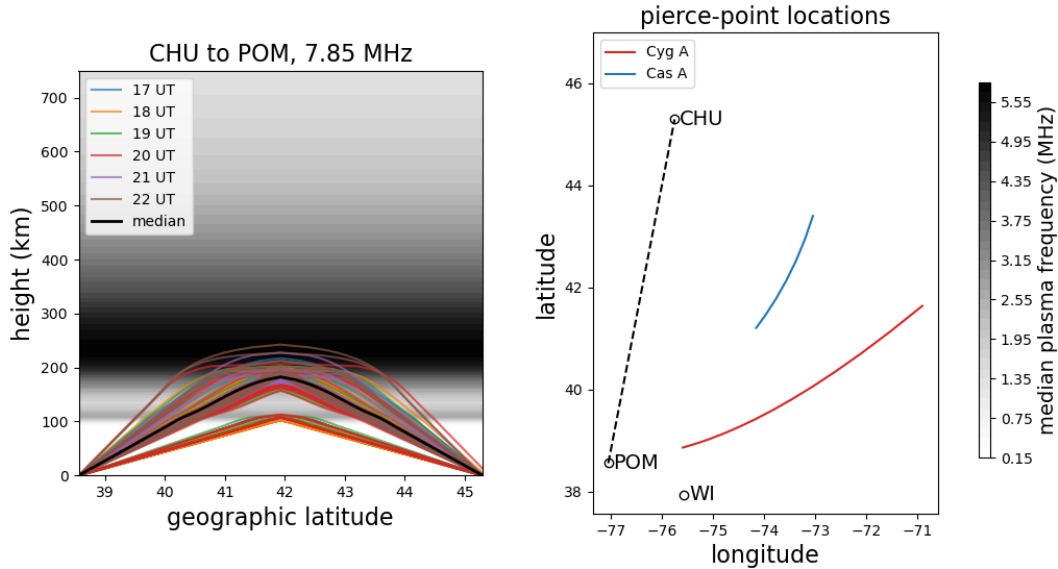


Figure 3. Left: The most likely ray path per hour during each collection date and time interval using a background ionosphere specified by the International Reference Ionosphere, constrained by parameters from the digisonde system at Wallops Island (WI). Each ray is color-coded by universal time. The grayscale image in the background is the median plasma frequency profile among all the collection dates/times. The black curve is the most likely ray path through this median profile. Right: Ionospheric pierce points at an altitude of 300 km from Pomonkey (POM) toward Cyg A (red) and Cas A (blue) during the data collections relative to the locations of the CHU radio station and the WI dynasonde. The path from CHU to POM is traced with a black dashed line.

253 the amplitude of the cross correlated voltages by the square root of the product of the
 254 received power (i.e., auto-correlation) at each antenna averaged over the same coherent
 255 integration time (see Fig. 1b). Thus, $C_k L$ values measured using 35 MHz observations
 256 of Cyg A and Cas A and/or dynasonde-based estimates of $C_k L$ can be used with esti-
 257 mates of F_e and θ to compute expected cross-correlation amplitudes and compared with
 258 observations.

259 **3.2 Observational Tests**

260 To estimate values of θ and F_e for the Oct./Nov. 2020 data collections, the Inter-
 261 national Reference Ionosphere (IRI) (Bilitza et al., 2014) constrained with parameters
 262 from the digisonde system near Wallops Island, Virginia was used to generate vertical
 263 profiles (5-km spacing) at one-hour intervals throughout the collection period. Using a
 264 simple ray tracing algorithm, the most likely signal path (with $N_{hop} = 1$) between CHU
 265 and DLITE-POM at the transmitted frequency of 7.85 MHz was estimated. These ray
 266 paths are plotted in the left panel of Fig. 3, color-coded by universal time. The median
 267 plasma frequency profile is shown in the background as a grayscale image.

268 While there are a few ray paths that only propagate within the E-region due to oc-
 269 casional sporadic-E, the vast majority travel through the lower portion of the F-region,
 270 usually well below the peak height. There is also not a clear trend with universal time,
 271 although the maximum heights of the 19 and 20 UT rays tend to be somewhat lower.
 272 The black curve within the figure shows the most likely path through the median N_e pro-

file, which also appears to be a fair representation of the typical path for all dates and times. For simplicity, the values of θ and F_e for this ray were used for all dates and times, which are 62.0° and 0.037, respectively. Here, it was assumed that θ is the complement of the initial elevation angle of the ray path. Assuming $\nu = 1.35$, it follows from equations (7)–(8) that $\sigma_{\Delta\phi}^2 = 8.54 \times 10^{-32} C_k L$ in this case.

To compare with the DLITE-based $C_k L$ calculations, the mean observed 7.85 MHz cross-correlation amplitude was computed within each time interval used to calculate $C_k L$, which are spaced by ~ 20 minutes. This was done by coherently averaging the complex cross correlations within each of these intervals, and then computing the amplitude of the result. As before (e.g., Fig. 1b), these cross-correlation amplitudes were then normalized by the mean received power within the same interval. The results are plotted as a function of time for each date in Fig. 4 for RHCP (black) and LHCP (gray). Horizontal black dotted lines indicate the value where $\sigma_{\Delta\phi} = 1$, which represents the case where the coherence length is equal to r_{eff} for the two DLITE antennas (approximately 220 m). Time series calculated with $C_k L$ values derived from Cyg A and Cas A are also plotted in red and blue, respectively.

While there is obviously not a one-to-one correspondence between the observed and estimated values, the DLITE-based values generally show the same level of incoherence as the data per day with a few exceptions (e.g., 26 and 28 Oct.). One should also note that the observed amplitudes will never be as close to unity as the low- $C_k L$ instances predict due to noise that is not correlated between the two antennas. Still, the correlation coefficient, r , between the observed values and the DLITE-based calculations is 0.2. This is not particularly strong, but significant nonetheless. To confirm this, the DLITE-based values were randomly resorted and the correlation coefficient was recalculated one hundred times. Among these, the 99th percentile was 0.1. In contrast, if the daily median values are compared, r increase to 0.6, which is consistent with the qualitative assessment above that the DLITE-based calculations reproduce the observed day-to-day variations better than the shorter timescale changes.

WI dynasonde-based values for the cross-correlation amplitude are also plotted in Fig. 4 (in green) but are not well correlated with the observed values with $r = 0.1$. Likewise, the correlation coefficient between the dynasonde-based $\log_{10} C_k L$ values and those from either Cyg A or Cas A was also 0.1. However, the daily median values of $\log_{10} C_k L$ were well correlated between the dynasonde and DLITE with $r \simeq 0.3$ –0.4, similar to what was found within the longer term study of Helmboldt and Zobotin (2022). Similarly, comparing the daily median values for the 7.85 MHz cross-correlation amplitude between the observations and dynasonde-based calculations gives $r \simeq 0.4$. This implies that while the WI-measured irregularity activity did not follow the same hour-by-hour pattern as those observed with DLITE, either at 7.85 or 35 MHz, the general level of activity per day was similar.

4 Discussion and Conclusions

The results presented here show that in the weak scattering case, which is the norm at mid-latitudes, the relatively simple MR79 model can be used to convert vertically integrated scintillation measurements at 35 MHz to estimates of skywave signal spatial coherence within the same region. This was demonstrated using measurements of the cross-correlation of a 7.85 MHz skywave signal between two antennas with an effective separation of ~ 220 m. While the coherence between the two is typically quite high, there are several instances where it drops low enough to infer that the coherence length was $\lesssim 220$ m. This is true of both the direct observations and the values calculated based on 35-MHz scintillations. This illustrates the potential utility of such scintillation measurements for applications such as site selection/system design for skywave systems that em-

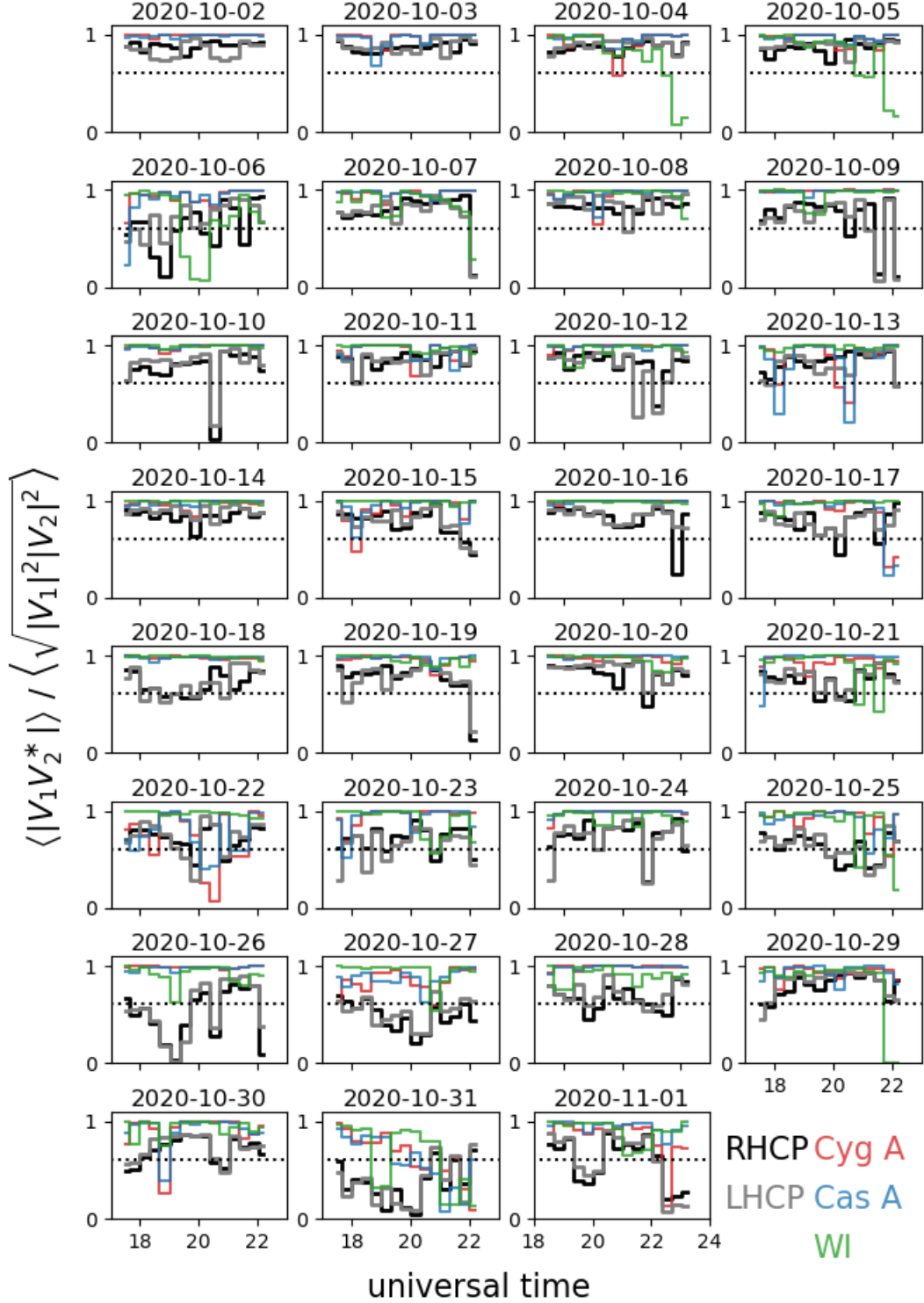


Figure 4. Time series of 7.85 MHz cross-correlation amplitudes within intervals of ~ 20 minutes per day of the campaign. Observed values are plotted in black and gray for right- and left-hand circular polarization, respectively. Estimates from $C_k L$ values derived from 35-MHz observations of Cyg A and Cas A are plotted in red and blue, respectively, and those derived from Wallops Island (WI) dyansonde parameters are plotted in green. The value at which the variance in the differential phase is unity, i.e., $\sigma_{\Delta\phi} = 1$, is represented by a horizontal black dotted line within each panel.

323 ploy spatial arrays of antenna, even at mid-latitudes where scattering is often relatively
324 weak.

325 This main result, however, is not without caveats. The agreement between the 7.85
326 MHz skywave observations and estimates based on DLITE scintillation measurements
327 are significantly but weakly correlated. While the general level of spatial coherence per
328 day is often reproduced relatively well, the agreement per time interval is not as good.
329 This is likely due in part to the physical separation between the locations probed by the
330 7.85 and 35 MHz observations, which is illustrated in the right panel of Fig. 3. The fact
331 that the results based on the WI dynasonde do not correlate significantly on an hourly
332 basis with the 7.85 MHz observations is somewhat consistent with this since it is at a
333 lower latitude than either the midpoint between CHU and Pomonkey or the ionospheric
334 pierce points associated with Cyg A or Cas A.

335 In addition, the results for Cyg A and Cas A often do not agree, and the $C_k L$ val-
336 ues derived from each typically differ by a factor of ~ 2 (Helmboldt et al., 2021). That
337 being said, the difference between the Cyg A and Cas A calculations is often smaller than
338 the difference between either of them and the observed 7.85 MHz cross-correlation am-
339 plitude as evidenced by the plots in Fig. 4. Thus, there must be limitations to this approach
340 that go beyond spatial variations in $C_k L$ within the region. These may include the as-
341 sumption of single values for θ and F_e as well as the fact that the lines of sight toward
342 the cosmic sources are moving while the HF ray path is essentially fixed. Other assump-
343 tions within the model calculations likely also play a role, including those used to con-
344 vert dynasonde parameters into $C_k L$.

345 Despite limitations, these results represent a promising step toward a better un-
346 derstanding of mid-latitude km-scale irregularities and a capability for estimating their
347 impact on HF skywave systems. DLITE scintillation measurements in particular are based
348 on observations of naturally occurring, cosmic radio sources, and thus have the poten-
349 tial to yield a completely passive method for assessing HF skywave channel quality within
350 a given mid-latitude region.

351 Acknowledgments

352 Digisonde parameters were obtained from the Global Ionosphere Radio Observatory ([https://](https://giro.uml.edu)
353 giro.uml.edu). Derived DLITE data products used within this publication are avail-
354 able via the Long Wavelength Array (LWA) data archive at [https://lwa10g.alliance](https://lwa10g.alliance.unm.edu/~dlite/chu)
355 [.unm.edu/~dlite/chu](https://lwa10g.alliance.unm.edu/~dlite/chu). Dynasonde parameters used within this study can be obtained
356 via SQL database query accessible at <http://surf.colorado.edu/login.dcc>. Instruc-
357 tions on how to obtain an account for database access are provided there. International
358 Reference Ionosphere software was obtained from <https://irimodel.org>. Development
359 and testing of the DLITE system were supported by the Defense Advanced Research Agency
360 (DARPA) Space Environment Exploitation (SEE) program. Research performed for this
361 project was supported by the Naval Innovative Science and Engineering (NISE) program
362 at the U.S. Naval Research Laboratory.

363 References

- 364 Bilitza, D., Altadill, D., Zhang, Y., Mertens, C., Truhlik, V., Richards, P., . . .
365 Reinisch, B. (2014, Feb). The International Reference Ionosphere 2012 - a
366 model of international collaboration. *Journal of Space Weather and Space*
367 *Climate*, 4, A07. doi: 10.1051/swsc/2014004
- 368 Carrano, C. S., Groves, K. M., & Rino, C. L. (2019). On the relationship be-
369 tween the rate of change of total electron content index (roti), irregular-
370 ity strength (ckl), and the scintillation index (s4). *Journal of Geophysi-*
371 *cal Research: Space Physics*, 124(3), 2099-2112. Retrieved from <https://>

- 372 [agupubs.onlinelibrary.wiley.com/doi/abs/10.1029/2018JA026353](https://doi.org/10.1029/2018JA026353) doi:
373 <https://doi.org/10.1029/2018JA026353>
- 374 Cohen, A. S., & Röttgering, H. J. A. (2009, August). Probing Fine-Scale Iono-
375 spheric Structure with the Very Large Array Radio Telescope. *Astron. J.*, *138*,
376 439-447. doi: 10.1088/0004-6256/138/2/439
- 377 DiLullo, C., Taylor, G. B., & Dowell, J. (2020). Using the long wavelength array
378 to search for cosmic dawn. *Journal of Astronomical Instrumentation*, *09*(02),
379 2050008. doi: 10.1142/S2251171720500087
- 380 Ellingson, S. W., Taylor, G. B., Craig, J., Hartman, J., Dowell, J., Wolfe, C. N.,
381 ... Weiler, K. W. (2013, May). The LWA1 Radio Telescope. *IEEE*
382 *Transactions on Antennas and Propagation*, *61*, 2540-2549. doi: 10.1109/
383 TAP.2013.2242826
- 384 Fletcher, A. C., Crabtree, C., Huba, J., Ganguli, G., & Siefiring, C. (2020). Early
385 time evolution of turbulence in the space environment by neutral beam injec-
386 tion. *Journal of Geophysical Research: Space Physics*, *125*(1), e2019JA027587.
387 (e2019JA027587 10.1029/2019JA027587) doi: [https://doi.org/10.1029/
388 2019JA027587](https://doi.org/10.1029/2019JA027587)
- 389 Ganguli, G., Crabtree, C., Fletcher, A. C., Rudakov, L., Richardson, A. S., Huba,
390 J., ... Lewis, C. D. (2019). Understanding and harnessing the dual elec-
391 trostatic/electromagnetic character of plasma turbulence in the near-earth
392 space environment. *Journal of Geophysical Research: Space Physics*, *124*(12),
393 10365-10375. doi: <https://doi.org/10.1029/2019JA027372>
- 394 Helmboldt, J. F., & Hurley-Walker, N. (2020). Ionospheric irregularities ob-
395 served during the gleam survey. *Radio Science*, *55*(10), e2020RS007106.
396 Retrieved from [https://agupubs.onlinelibrary.wiley.com/doi/abs/
397 10.1029/2020RS007106](https://agupubs.onlinelibrary.wiley.com/doi/abs/10.1029/2020RS007106) (e2020RS007106 10.1029/2020RS007106) doi:
398 <https://doi.org/10.1029/2020RS007106>
- 399 Helmboldt, J. F., Lazio, T. J. W., Intema, H. T., & Dymond, K. F. (2012, Febru-
400 ary). High-precision measurements of ionospheric TEC gradients with the Very
401 Large Array VHF system. *Radio Science*, *47*, 0. doi: 10.1029/2011RS004883
- 402 Helmboldt, J. F., Markowski, B. B., Bonanno, D. J., Clarke, T. E., Dowell, J., Hicks,
403 B. C., ... Taylor, G. B. (2021). The deployable low-band ionosphere and
404 transient experiment. *Radio Science*, *56*(7), e2021RS007298. (e2021RS007298
405 2021RS007298) doi: <https://doi.org/10.1029/2021RS007298>
- 406 Helmboldt, J. F., & Zobotin, N. (2022). An observed trend between mid-latitudes
407 km-scale irregularities and medium-scale traveling ionospheric disturbances.
408 *Radio Science*, *57*(5), e2021RS007396. doi: [https://doi.org/10.1029/
409 2021RS007396](https://doi.org/10.1029/2021RS007396)
- 410 Hicks, B. C., Paravastu-Dalal, N., Stewart, K. P., Erickson, W. C., Ray, P. S., Kas-
411 sim, N. E., ... Weiler, K. W. (2012, October). A Wide-Band, Active Antenna
412 System for Long Wavelength Radio Astronomy. *Publications of the Astronomi-
413 cal Society of the Pacific*, *124*, 1090-1104. doi: 10.1086/668121
- 414 Jacobson, A. R., & Erickson, W. C. (1992, April). A method for characterizing tran-
415 sient ionospheric disturbances using a large radiotelescope array. *Astron. As-
416 trophys.*, *257*, 401-409.
- 417 Kintner, P. M., Ledvina, B. M., & de Paula, E. R. (2007). Gps and iono-
418 spheric scintillations. *Space Weather*, *5*(9). Retrieved from [https://
419 agupubs.onlinelibrary.wiley.com/doi/abs/10.1029/2006SW000260](https://agupubs.onlinelibrary.wiley.com/doi/abs/10.1029/2006SW000260) doi:
420 <https://doi.org/10.1029/2006SW000260>
- 421 Loi, S. T., Murphy, T., Cairns, I. H., Menk, F. W., Waters, C. L., Erickson, P. J.,
422 ... Williams, C. L. (2015, May). Real-time imaging of density ducts be-
423 tween the plasmasphere and ionosphere. *Geophysical Research Letters*, *42*(10),
424 3707-3714. doi: 10.1002/2015GL063699
- 425 Mevius, M., van der Tol, S., Pandey, V. N., Vedantham, H. K., Brentjens, M. A., de
426 Bruyn, A. G., ... Zaroubi, S. (2016). Probing ionospheric structures using the

- 427 lofar radio telescope. *Radio Science*, 51(7), 927-941. Retrieved from [https://](https://agupubs.onlinelibrary.wiley.com/doi/abs/10.1002/2016RS006028)
428 agupubs.onlinelibrary.wiley.com/doi/abs/10.1002/2016RS006028 doi:
429 <https://doi.org/10.1002/2016RS006028>
- 430 Nickisch, L. J., St. John, G., Fridman, S. V., Hausman, M. A., & Coleman, C. J.
431 (2012). Hicirf: A high-fidelity hf channel simulation. *Radio Science*, 47(4). doi:
432 <https://doi.org/10.1029/2011RS004928>
- 433 Rino, C. L. (1979). A power law phase screen model for ionospheric scintillation: 1.
434 weak scatter. *Radio Science*, 14(6), 1135-1145. doi: [https://doi.org/10.1029/](https://doi.org/10.1029/RS014i006p01135)
435 [RS014i006p01135](https://doi.org/10.1029/RS014i006p01135)
- 436 Tatarskii, V. I. (1961). *Wave Propagation in Turbulent Medium*. McGraw-Hill.
- 437 Taylor, G. B., Ellingson, S. W., Kassim, N. E., Craig, J., Dowell, J., Wolfe, C. N.,
438 ... Wood, D. L. (2012, December). First Light for the First Station of the
439 Long Wavelength Array. *Journal of Astronomical Instrumentation*, 1, 50004.
440 doi: 10.1142/S2251171712500043
- 441 Zaboltn, N. A., & Wright, J. W. (2001, July). Ionospheric irregularity diagnos-
442 tics from the phase structure functions of MF/HF radio echoes. *Radio Science*,
443 36(4), 757-771. doi: 10.1029/2000RS002512